Proper Generalized Decomposition with time adaptive space separation for transient wave propagation problems in separable domains

Dimitri Goutaudier, Laurent Berthe, Francisco Chinesta

Proper Generalized Decomposition with time adaptive space separation for transient wave propagation problems in separable domains

Dimitri Goutaudier[a,*], Laurent Berthe[a], Francisco Chinesta[b]

[a] *PIMM, Arts et Métiers Institute of Technology, CNRS, HESAM, CNAM, 151 boulevard de l'Hôpital, 75013 Paris, France*
[b] *ESI GROUP Chair @ PIMM, Arts et Métiers Institute of Technology, France*

Abstract

Transient wave propagation problems may involve rich discretizations, both in space and in time, leading to computationally expensive simulations, even for simple spatial domains. The Proper Generalized Decomposition (PGD) is an attractive model order reduction technique to address this issue, especially when the spatial domain is separable. In this work, we propose a space separation with a time adaptive number of modes to efficiently capture transient wave propagation in separable domains. We combine standard time integration schemes with this original space separated representation for empowering standard procedures. The numerical behavior of the proposed method is explored through several 2D wave propagation problems involving radial waves, propagation on long time analyses, and wave conversions. We show that the PGD solution approximates its standard finite element solution counterpart with acceptable accuracy, while reducing the storage needs and the computation time (CPU time). Numerical results show that the CPU time per time step linearly increases when refining the mesh, even with implicit time integration schemes, which is not the case with standard procedures.

Keywords: Proper Generalized Decomposition (PGD); Transient wave propagation; Time adaptive space separation; Separable domain; Scalar wave equation; Elastodynamics

1. Introduction

Transient wave propagation analyses are often necessary to fully understand the dynamic behavior of a mechanical system or the details of a mechanical process. This is notably the case for laser shock processes that consist in applying a sudden pressure, up to several GPa, locally on the surface of a material part [1,2]. The outcomes of understanding these processes at the wave propagation level are important to optimize the laser parameters [3,4] or to determine the mechanical properties of the medium [5,6]. These laser shock processes are numerically explored through parametric studies on transient wave propagation problems in plate domains, by varying the loading parameters, the material properties or the mechanical behavior laws [7,8]. It would be beneficial to reduce the computation time and the storage requirements associated to these numerous simulations.

* Corresponding author.
E-mail address: dimitri.goutaudier@ensam.eu (D. Goutaudier).

Many numerical tools have been developed over the past decades to solve transient wave propagation problems. The classical approach consists in using a time integration scheme with the Finite Element Method (FEM). It is however difficult to obtain accurate solutions with this method because of numerical dispersion and dissipation, resulting in non-physical wave velocities, period elongations and amplitude decays [9]. In addition, the error between the exact and the numerical solutions may severely increase as the waves travel in the medium, because of spurious numerical high frequency oscillations related to the Gibb's phenomenon. The numerical solution can straightforwardly be improved by refining the mesh and by carefully selecting the time step according to both the element size and the selected time integration scheme [10]. Instead of refining the mesh, which increases the computation time, another approach is to select an appropriate time integration scheme with good dissipation and dispersion properties. For instance the Bathe method is an effective implicit time integration scheme for computing accurate transient wave propagation solutions [11,12]. The Spectral Element Method (SEM) has been developed to reduce the numerical dispersion with respect to the standard FEM [13,14]. Instead of using standard finite elements, high-order Lagrangian-based finite elements with specific integration points are used to build a diagonal mass matrix. Consequently, the SEM can be effective for computing transient wave propagation solutions in explicit time integration. Similarly, Lagrangian-based finite elements enriched with harmonic functions have been proposed to significantly improve the accuracy with respect to standard finite elements [15]. Finally, approaches based on discontinuous finite element formulations have been developed to solve transient wave propagation problems involving sharp gradients. For instance the Time Discontinuous Galerkin method (TDG) using space–time finite elements is effective for reducing high frequency spurious oscillations [16].

The computation time and the storage requirements of these methods significantly increase when rich discretizations are used to study the details of the wave propagation. Reduced order modeling is an active field of research offering promising approaches to deal with this issue. In the present study we do not intend to propose a new model order reduction technique. We focus on the Proper Generalized Decomposition (PGD) which is an attractive technique when the geometry of the domain is separable, as for the laser shock simulations described above. The PGD has been developed to overcome the so-called curse of dimensionality when it comes to solve a multi-dimensional problem [17,18]. This technique consists in computing on the fly a separated form representation of the solution, directly from the weak formulation of the problem. The main idea is to solve several problems of lower dimensions than the initial problem to alleviate the computational costs. When it comes to solve time-dependent partial differential equations, the PGD is usually implemented by considering the space–time separation presented in [19]:

$$u(x, y, t) \approx \sum_{i=1}^{M} S_i(x, y) T_i(t) \tag{1}$$

where u represents a time-dependent scalar field defined over a 2D space domain. This space–time separation avoids using a time incremental solver, by analogy with the Proper Orthogonal Decomposition (POD). If the length of the sum M is small (between 10–100 for instance) then the time dependent solution can be stored with significantly less storage capacities. Unlike the POD that requires snapshots of the solution [20], no prior knowledge on the solution needs to be known with the PGD. Over the last decade, the space–time separation has led to a plurality of demonstrations that the PGD computes accurate solutions faster than standard incremental solvers. This technique has been applied to a wide range of problems in different branches of physics: in rheology [21], thermal analysis [22], kinetic theory of complex fluids [23], and even in quantum chemistry [24]. From a mathematical standpoint, several works [25,26] proved convergence results of the PGD algorithm with the space–time separation for problems involving elliptic operators. In elastodynamics, the space–time separation has been used to compute vibration responses up to the medium frequency domain [27,28]. However, difficulties have been experienced when the problem equations involve hyperbolic operators [23], which is typically the case with a wave equation. Therefore very few works have addressed the topic of wave propagation with the PGD. In [29,30] the authors presented a space–time separation within a TDG framework to remove spurious oscillations associated to transient wave propagation simulations. They applied their method to a 2D transient elastodynamic problem with a rectangular geometry, and they reported poor convergence results when using a standard PGD algorithm. To improve the numerical performances in terms of storage gain, the authors proposed a recompactification strategy to compute a lower rank approximation of the solution. However, this technique requires an experimented analyst to select the so-called auxiliary rank parameter of the method. In addition, difficulties are reported to compute the solution faster

than with a standard TDG technique. As mentioned in their work, the computational cost associated to their method could be improved by considering a complete variables separation strategy, both in space and in time. However, to our knowledge, this approach has not been investigated.

In this context, the aim of this paper is not proposing an algorithm making radically faster or better, the existing algorithms already perform well, and from that point of view the one here proposed reduces storage needs and speed-up calculations. Here the main and crucial ingredient is the space separation, because nowadays engineered materials may involve thin coatings, geometries sometimes composed of extremely fine plies, and then when solutions are rich throughout the also rich domain thickness, 3D discretizations are sometimes unattainable. This is particularly the case for laser shock processes on composite laminate targets [3,5,7]. In this study, we combine standard integrators with an original space separated representation for empowering standard procedures. The proposed methodology is here applied to 2D domains, with stringent loading configurations for the space separation, to analyze its numerical behavior. Therefore, the results do not reflect the entire potential of the method for reducing the CPU time and the storage needs for computationally intensive problems. Future research will be devoted to 3D transient elastodynamic problems in composite laminates.

The paper is organized as follows. In Section 2 we present a time adaptive space separation strategy. We discuss the main features of this approach and we highlight its limitations. We present an implementation of this formulation to the 2D scalar wave equation, but the same methodology can be employed for the 2D elastodynamics equations. Three commonly employed time integration schemes for wave propagation analyses are implemented: the central difference method (explicit, conditionally stable), the Newmark trapezoidal rule and the Bathe method (implicit, unconditionally stable). In Section 3 we explore the numerical behavior of the proposed PGD algorithm on several 2D problems involving radial waves, multiple reflections, propagation on long time analyses, and wave conversions. We compare the obtained results with the exact solution when available, and to numerical solutions computed with a standard finite element method using the same time integration scheme. Finally we discuss the numerical performances of the proposed approach in terms of storage gain and computation time.

2. Formulation of the method

In this section we introduce a new PGD formulation adapted to transient wave propagation problems in separable domains. The main idea is to perform a space separation at each time increment with an adaptive number of modes. Then we compare the advantages and the limitations of this approach with respect to PGD methods based on a conventional space–time separation. Finally we present the implementation of this formulation to the 2D scalar wave equation.

2.1. Space variables separation at each time increment

It is well known [31] that the solution of the 1D wave equation $\ddot{u} - c^2 u'' = 0$ is under the form $u(x,t) = f(x-ct) + g(x+ct)$. This result evidences that space and time variables are linked into phase variables $x \pm ct$ to describe the propagation of a disturbance. This observation could partially explain the difficulties encountered to implement standard PGD algorithms with a space–time separation for wave propagation problems [23]. Instead, we propose to implicitly separate some phase variables related to each spatial direction. This can be done by performing a standard space variables separation, but at each time increment t_k, yielding in the 2D case to the following separated form representation:

$$u(x, y, t_k) \approx \sum_{i=1}^{M(t_k)} \phi_i(x, t_k)\psi_i(y, t_k) \tag{2}$$

The fields $\phi_i(x,t)$ and $\psi_i(y,t)$ are referred as the ith PGD modes in x- and y-directions, respectively. An important feature of (2) is the adaptive number of modes $M(t)$ used to increase the enrichment of the numerical solution when needed, depending on the complexity of the wave field at a given instant. This number is expected to evolve as the waves travel within the medium, reflect at the boundaries, and exhibit sharp spatial variations, as discussed later in Section 2.2.

This separated form representation, called time adaptive space separation in the following, is built up on the fly, directly from the considered wave equation, with a standard PGD algorithm based on a space separation at each

time increment (see Section 2.4). Any time integration scheme compatible with the standard finite element method framework can be used. The PGD solution may then be computed faster than its standard FEM solution counterpart (see Section 3.1), by solving multiple 1D problems in space rather than a single 2D problem, and with less storage needs, as explained in Section 2.3.

This formulation is applicable when the spatial domain Ω is separable [32]. In 2D, it limits the study to rectangular domains $\Omega = \Omega_x \times \Omega_y$, and in 3D to domains with an extrusion direction $\Omega = \Omega_{xy} \times \Omega_z$ (plate, cylinder etc.). In fact, more complex geometries can be considered by using adequate geometrical transformations [33]. It is also important to mention that this space separation cannot exactly represent a wave front as simple as a circle with a finite number of terms in (2). Hence, at first sight, radial waves seem difficult to be captured with this approach. Yet the numerical results demonstrate that the proposed method is actually effective in the context of numerical approximations for capturing complicated wave fields, including radial waves, with a moderate number of modes (typically 20 in the studied use cases). This can be explained by thinking of the proposed PGD algorithm as performing a Truncated Singular Values Decomposition (TSVD) of the wave field discretized in space at each time increment. It is well known that the TSVD provides accurate low rank approximations in many situations [34]. The results presented in Section 3 suggest that the proposed method is capable of inheriting this good property, although it is known that the PGD usually requires higher ranks M than the TSVD [30].

2.2. Time adaptive enrichment

In this work we emphasize the importance of using an adaptive number of modes $M(t)$ through the simulation, instead of selecting a fixed rank M before the computation. The objective of this feature is to enrich the solution through time when needed, as the waves are initiated by an imposed loading, travel in the medium or interact with the boundaries.

First, similarly to the TSVD, it can be expected that the sharper the wave field is, for instance because of an imposed loading, the more modes will be needed to approximate the solution. This is illustrated on simple examples on Fig. 1a to c. $M = 25$ terms are necessary with the TSVD to approximate the surface displayed on Fig. 1a with a relative error of 10^{-10}, while only $M = 4$ terms are sufficient to approximate the smoother surface displayed on Fig. 1b with the same relative error.

Second, the propagative behavior of the solution is also expected to affect the number of terms in the sum (2). More precisely, it can be anticipated that $M(t)$ will increase as the waves expand in the domain. This can be illustrated through the following fictive situation. Consider the diagonal propagation of a linear wave front in a square domain, see Fig. 1d, uniformly discretized in space. The coordinates of the nodes are (x_i, y_j) and the discretized wave field at time step $t_k = k\Delta t$ is represented by the matrix with general coefficient $U_{ij}^{(k)} = u(x_i, y_j, t_k)$. Suppose that the wave front is initiated at time t_1, so that $u(x_1, y_1, t_1) = 1$, and that it diagonally propagates towards the bottom right corner (x_n, y_n) until time t_n, without interacting with the boundaries (ideal absorption). At each new time increment the wave front expands and reaches new nodes, so that the discretized wave field at any time $t_k \leq t_n$ is under the form:

$$U^{(k)} = \begin{bmatrix} \tilde{I}_k & 0_{k,n-k} \\ 0_{n-k,k} & 0_{n-k,n-k} \end{bmatrix} \tag{3}$$

where $\tilde{I}_k$ is a unit anti-diagonal square matrix of size k. It is straightforward to notice that $\tilde{I}_k \tilde{I}_k^T = \tilde{I}_k^T \tilde{I}_k = I_k$, with I_k the identity matrix of size k. It follows that the rank of the discretized wave field matrix linearly increases with time as the length of the wave front expands when traveling:

$$\text{rank}(U^{(k)}) = k \text{ for } t_k \leq t_n \tag{4}$$

Of course, this fictive example is a worst case scenario in the sense that no low rank approximation can be used to accurately represent this extremely sharp wave front propagation (sudden 0 to 1 discontinuity at each time step). Indeed, all the singular values of $U_{ij}^{(k)}$ are equal to 1 hence there is no truncation order characterized by a jump in the singular values, as observed with the examples presented in Fig. 1c. In practice, it is observed that $M(t)$ generally increases as the waves expand, but up to acceptable values leading to a storage gain with respect to conventional methods.

In light of this discussion, it becomes clearer that an adaptive number of modes is necessary for transient wave propagation problems. On one hand, if the number of modes is not sufficient to describe the solution at a given

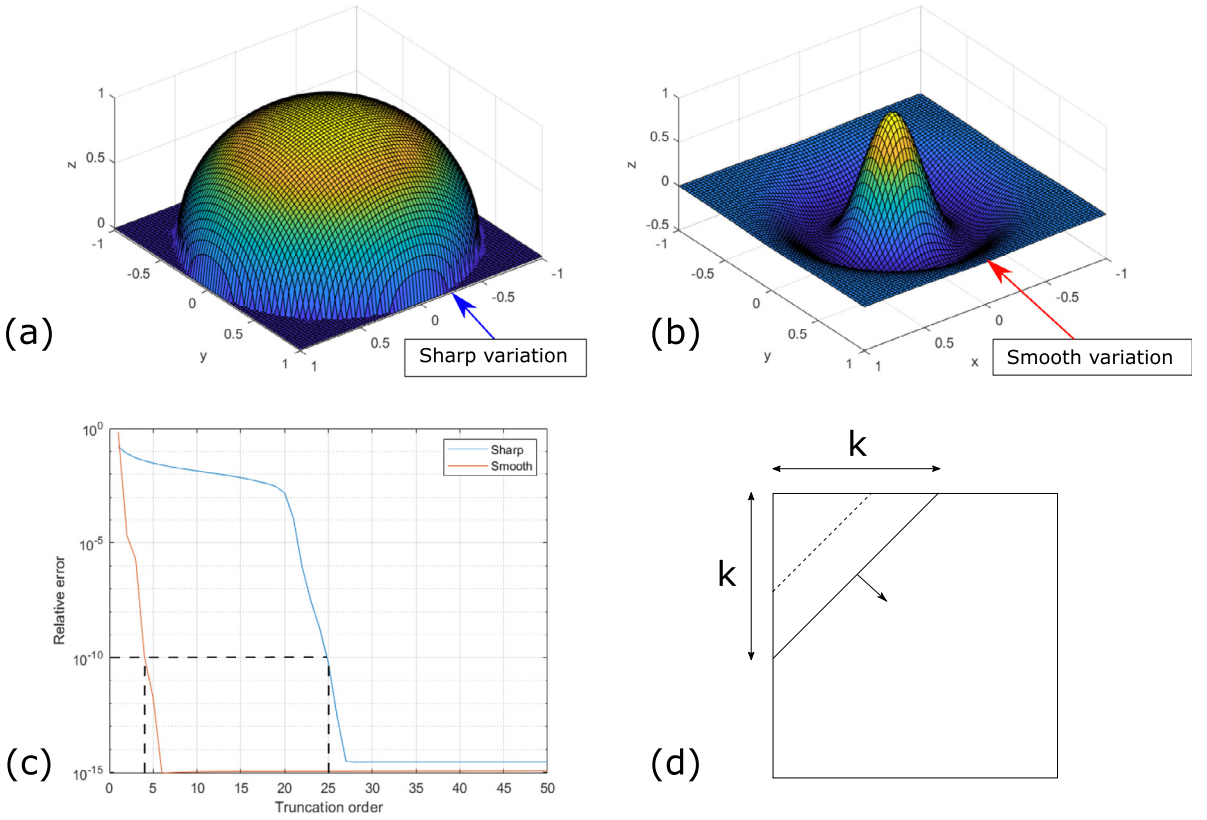

Fig. 1. Surfaces with (a) sharp or (b) smooth variations (discretization with 75 points in each direction). (c) Relative error between the TSVD approximations and the exact surfaces depending on the truncation order. (d) Linear wave front diagonally propagating in a square domain with absorbing boundaries.

instant, the numerical errors will accumulate through the simulation and will severely compromise the accuracy. On the other hand, if the number of modes is too high the computation of the PGD approximation will not be effective in terms of computation time and memory capacities.

2.3. Storage gain analysis

The storage gain, associated to a PGD formulation with respect to a standard time incremental finite element formulation, can be evaluated as the ratio of the amount of data to write the solution on disk. To do so, consider a rectangular spatial domain with N_x and N_y discretization points along each direction, and a number N_t of output time steps to write the solution. With a time incremental finite element approach, $N_x N_y$ nodal values of the wave field must be stored at each time step. Therefore the total amount of data to be stored is $N_x N_y N_t$. On the other hand, with the space–time separation (1) the total amount of data to be stored is $M(N_x N_y + N_t)$, and it is $\overline{M}(N_x + N_y)N_t$ with the time adaptive space separation (2), where $\overline{M}$ is the mean number of modes over the selected output time steps. Three cases illustrate the storage gain associated to the space–time separation:

$$\text{storage gain with space–time separation} \approx \begin{cases} N/M & \text{if } N_x = N_y = N_t = N \\ N_t/M & \text{if } N_x = N_y = N \text{ and } N_t \ll N \\ N^2/M & \text{if } N_x = N_y = N \text{ and } N_t \gg N \end{cases} \tag{5}$$

Regarding the time adaptive space separation presented in this paper, the number of time steps N_t cancels out in any case, hence the storage gain is given by:

$$\text{storage gain with time adaptive space separation} = (N/2)/\overline{M} \text{ if } N_x = N_y = N \tag{6}$$

An important storage gain can be obtained with both approaches if the PGD algorithm successfully computes a low rank approximation of the solution. Eq. (5) shows that the storage gain may increase with the space–time separation when considering longer time analyses, which is not the case with the time adaptive space separation. However, it is not guaranteed that a low rank approximation can be computed with the space–time separation for transient wave propagation problems, as indicated in Section 2.1 and as reported in [30]. On the contrary, the numerical results presented in Section 3 show that the time adaptive space separation effectively computes low rank approximations, and reveal that the mean number of modes $\overline{M}$ stabilizes when considering longer time analyses. It is also found that $\overline{M}$ stabilizes when refining the mesh, which indicates that more accurate solutions are computed with more storage gain.

2.4. Implementation on the 2D scalar wave equation

The propagation of a scalar wave in a 2D rectangular domain Ω with free contour Γ and null initial conditions is governed by the following equations [31]:

$$\begin{cases} \frac{1}{c^2}\ddot{u} - \Delta u = f & \text{for } (x, y, t) \in \Omega \times]0, T] \\ \frac{\partial u}{\partial n} = 0 & \text{for } (x, y, t) \in \Gamma \times]0, T] \\ u(x, y, 0) = 0, \dot{u}(x, y, 0) = 0 & \text{for } (x, y) \in \Omega \end{cases} \tag{7}$$

where u is the field variable, c is the wave velocity (assumed constant for simplicity), and f is a source term with a separated form representation $f(x, y, t) = g(x, t)h(y, t)$.

The first step is to get the weak formulation of this problem. To do so, we multiply the first equation of (7) by an arbitrary test field u^* and we use Green's first identity associated with the second equation of (7), which yields:

$$\int_\Omega u^* \ddot{u} + \int_\Omega c^2 \nabla u^* \nabla u = \int_\Omega c^2 u^* f \tag{8}$$

The second step is to discretize equation (8) in time with a time integration scheme. For the purpose of clarity we consider here the central difference method with a constant time step Δt. The time increments are noted $t_k = k\Delta t$. Assuming that the solutions at times t_{k-1} and t_k are known, the equation to be solved at t_{k+1} is:

$$\int_\Omega u^* \frac{u^{k+1} - 2u^k + u^{k-1}}{\Delta t^2} + \int_\Omega c^2 \nabla u^* \nabla u^k = \int_\Omega c^2 u^* f^k \tag{9}$$

Then a standard PGD algorithm with a space separation is used on Eq. (9) to build the separated form representation of the unknown field u^{k+1}. This latter is ultimately approximated under the form:

$$u^{k+1}(x, y) \approx \sum_{i=1}^{M_{k+1}} \phi_i^{k+1}(x) \psi_i^{k+1}(y) \tag{10}$$

where a separate finite element discretization is used for each spatial direction to compute the PGD modes. More precisely, by noting P and Q the shape functions used for each spatial direction (linear 1D elements in this study), the finite element discretization in each spatial direction at time t_{k+1} reads:

$$\phi_i^{k+1}(x) \approx P(x)^T \Phi_i^{k+1} \tag{11}$$

$$\psi_i^{k+1}(y) \approx Q(y)^T \Psi_i^{k+1} \tag{12}$$

where Φ_i^{k+1} and Ψ_i^{k+1} are the vectors containing the nodal values of the spatial modes ϕ_i and ψ_i at time t_{k+1}, respectively.

2.5. Iterative enrichment procedure

The PGD algorithm computes the approximation (10) iteratively, by adding new pairs $(\phi_i^{k+1}, \psi_i^{k+1})$ to the solution within an enrichment loop. The number of modes M_{k+1} is automatically selected with an enrichment criterion. Each new pair is computed with a fixed point strategy within a stagnation loop. In practice these different sequences are

as follows. Assuming that the first $n-1$ terms of the sum (10) are known, the unknown field is enriched with a new pair:

$$u_n^{k+1} = u_{n-1}^{k+1} + \phi\psi \tag{13}$$

The problem becomes to find a new pair (ϕ, ψ) satisfying the weak formulation. By injecting (13) in (9), and by moving all the known terms to the right hand side of the equation, the new pair must satisfy:

$$\int_\Omega u^*\phi\psi = -\int_\Omega u^* u_{n-1}^{k+1} + 2\int_\Omega u^* u^k - \int_\Omega u^* u^{k-1} - \int_\Omega (c\Delta t)^2 \nabla u^* \nabla u^k + \int_\Omega (c\Delta t)^2 u^* f^k \tag{14}$$

This nonlinear problem is solved with a fixed point method. First the field ψ is assumed known and the arbitrary test field is taken under the form $u^* = \phi^*\psi$. Each integral over the plate domain is separated as a product of 1D integrals and the nodal approximations (11)–(12) are used. It results in a 1D problem in ϕ consisting in the following linear system to be solved:

$$\left[\sum_{i=1}^{n_A} \left(\Psi^T A_2^i \Psi\right) A_1^i\right] \Phi = \sum_{i=1}^{n_B} B_1^i (B_2^i)^T \Psi \tag{15}$$

where Φ and Ψ are the vectors of the nodal values of ϕ (unknown) and ψ (known), respectively. The operators involved in this equation are given in the Appendix. The same form of linear system is obtained when considering another time integration scheme or for the 2D elastodynamics equations. Then, ϕ is assumed known with the previously calculated approximation and the test field is taken under the form $u^* = \phi\psi^*$. The equations are then manipulated in the exact same manner, leading to a 1D problem in ψ consisting in the following linear system to be solved:

$$\left[\sum_{i=1}^{n_A} \left(\Phi^T A_1^i \Phi\right) A_2^i\right] \Psi = \sum_{i=1}^{n_B} B_2^i (B_1^i)^T \Phi \tag{16}$$

This alternative resolution in ϕ and in ψ is repeated until convergence. More precisely, by denoting $(\phi^{(s)}, \psi^{(s)})$ the pair calculated at the iteration s of the fixed point method, the stagnation criterion reads:

$$\left[\frac{\int_\Omega |\phi^{(s)}\psi^{(s)} - \phi^{(s-1)}\psi^{(s-1)}|^2}{\int_\Omega |\phi^{(s-1)}\psi^{(s-1)}|^2}\right]^{1/2} < \epsilon \tag{17}$$

where ϵ is a threshold value selected by the user. The enrichment loop over the number of pairs n is ultimately stopped when the following enrichment criterion is reached:

$$\left[\frac{\int_\Omega |u_n^{k+1} - u_{n-1}^{k+1}|^2}{\int_\Omega |u_1^{k+1}|^2}\right]^{1/2} < \tilde{\epsilon} \tag{18}$$

where $\tilde{\epsilon}$ is another threshold value selected by the user. This criterion leads to a different length of the sum (10) depending on the complexity of the solution at the considered time increment. The convergence can be evaluated by using different error indicators [35–37]. However, in general, the one based on the stagnation works reasonably in most of the applications. The influence of the criteria (17)–(18) on the accuracy and the numerical behavior of the PGD solution is investigated in Section 3.

2.6. Time integration schemes for wave propagation analyses

The implementation of the proposed method has been introduced in Section 2.4 with the central difference method, which is the second order accurate explicit scheme with the largest stability condition when combined with the finite element method [10]. The advantage of this scheme, when combined with the finite element method, is that the stiffness matrix does not need to be factorized and the mass matrix can be lumped, which results in a diagonal linear system to be solved at each time step [38]. However, as reported in Section 3.5, this time integration scheme is found to be less relevant in the proposed PGD framework. Indeed, the left hand side operators (15)–(16)

are computed at each iteration within the enrichment and stagnation loops, while the left hand side operator (the mass matrix) is computed once and for all with the finite element method, before the time incremental resolution.

On the contrary, the proposed PGD framework becomes more efficient when implicit time integration schemes are employed, which involve consistent matrices to be inverted at each time step. The alternative resolution of 1D problems with the PGD may then become more efficient than a single resolution of a 2D problem with the FEM. Therefore, we propose to explore the performances of the proposed formulation with two widely used implicit time integration schemes for wave propagation analyses: the Newmark trapezoidal rule [10] and the Bathe method [11]. These schemes are defined as follows:

- In the Newmark trapezoidal rule the equations used are:

$$\dot{u}^{k+1} = \dot{u}^k + \left[(1-\delta)\ddot{u}^k + \delta\ddot{u}^{k+1}\right]\Delta t \tag{19}$$

$$u^{k+1} = u^k + \dot{u}^k\Delta t + \left[\left(\frac{1}{2}-\alpha\right)\ddot{u}^k + \alpha\ddot{u}^{k+1}\right]\Delta t^2 \tag{20}$$

  with $\delta = 0.5$ and $\alpha = 0.25$.
- In the Bathe method the following equations are employed:

$$\dot{u}^{k+1/2} = \dot{u}^k + (\ddot{u}^k + \ddot{u}^{k+1/2})\frac{\Delta t}{4} \tag{21}$$

$$u^{k+1/2} = u^k + (\dot{u}^k + \dot{u}^{k+1/2})\frac{\Delta t}{4} \tag{22}$$

$$\dot{u}^{k+1} = \frac{1}{\Delta t}u^k - \frac{4}{\Delta t}u^{k+1/2} + \frac{3}{\Delta t}u^{k+1} \tag{23}$$

$$\ddot{u}^{k+1} = \frac{1}{\Delta t}\dot{u}^k - \frac{4}{\Delta t}\dot{u}^{k+1/2} + \frac{3}{\Delta t}\dot{u}^{k+1} \tag{24}$$

3. Numerical results

In this section, we present the performances of the time adaptive space separation for several transient wave propagation problems. First, we consider a pre-stressed membrane with a concentrated impact loading in its center. We study the convergence properties of the PGD solution with comparisons to the exact solution and to a standard 2D finite element solution. Three different time integration schemes are tested. Then, we solve a water ripple propagation problem and we focus on long time analyses to describe the numerical behavior of the PGD solution. Finally, we study a 2D transient elastodynamic problem representative of a laser shock on a metallic target. We study in this last example the effect of varying the concentration of the loading, both in space and in time, on the performances of the proposed approach.

3.1. Standard 2D FEM solution counterpart of the PGD solution

The objective of this numerical study is to demonstrate that the proposed PGD formulation computes as accurate transient wave propagation solutions as the standard finite element approach, but faster and with less storage needs. In order to assess the influence of the space separation, we systematically compare the PGD solution to its so-called FEM solution counterpart. As described in Section 2.4, we use a finite element discretization for each spatial direction with 2-node linear elements to compute the PGD solution. Therefore, the FEM solution counterpart is computed with standard 4-node quadrilateral elements, with the same total number of degrees of freedom. As an example, the finite element discretization associated to the scalar wave equation (7) with $f = 0$ is given by [10]:

$$M\ddot{U} + c^2KU = 0 \tag{25}$$

where U is the vector containing the nodal values of the solution, M and K are the mass and stiffness matrices, and the contribution to these matrices of element (e) with domain $\Omega^{(e)}$ is:

$$M^{(e)} = \int_{\Omega^{(e)}} (H^{(e)})^T H^{(e)} \tag{26}$$

$$H^{(e)} = \int_{\Omega^{(e)}} (\nabla H^{(e)})^T (\nabla H^{(e)}) \tag{27}$$

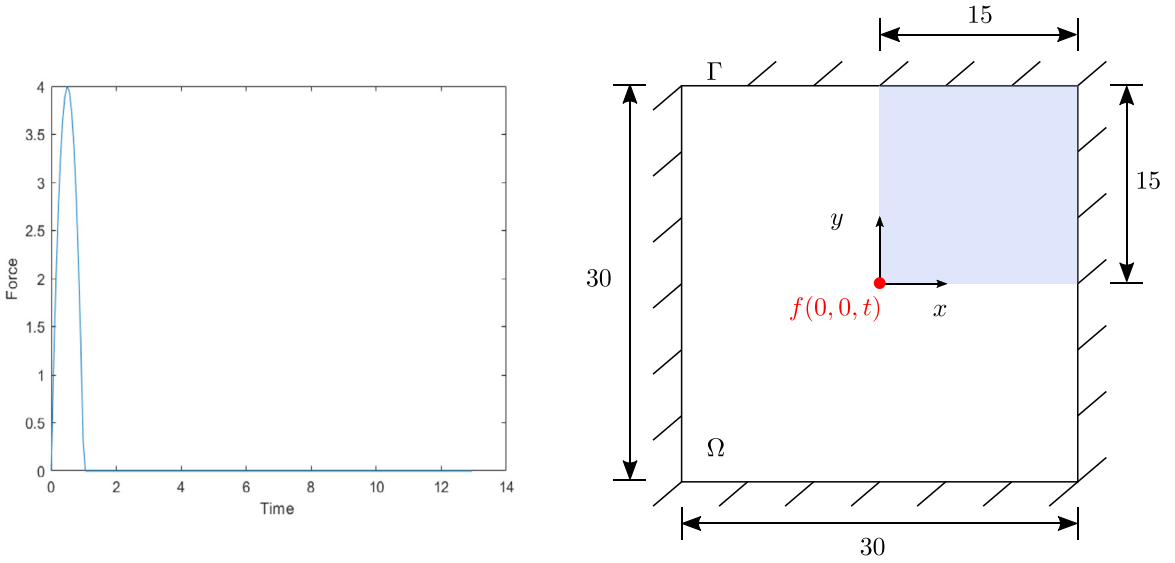

Fig. 2. Pre-stressed membrane with concentrated impact force. Numerical results are displayed on blue area.

where $H^{(e)}$ is the element interpolation matrix. The matrices M and K are computed from the elementary matrices $M^{(e)}$ and $K^{(e)}$ with a standard summation process. Eq. (25) is then discretized in time with the same time integration scheme used to compute the PGD solution.

3.2. Impacted pre-stressed membrane

We consider a pre-stressed membrane impacted in its center, see configuration on Fig. 2, for which the transverse displacement is governed by the following set of equations:

$$\begin{cases} \frac{1}{c^2}\ddot{u} - \Delta u = f(0,0,t) & \text{for } (x,y,t) \in \Omega \times]0,T] \\ u(x,y,t) = 0 & \text{for } (x,y,t) \in \Gamma \times]0,T] \\ u(x,y,0) = 0, \dot{u}(x,y,0) = 0 & \text{for } (x,y) \in \Omega \end{cases} \tag{28}$$

with $f(0,0,t) = 4(1-(2t-1)^2)H(1-t)$ where $H(t)$ is the unit step function, and we select a unit wave velocity $c = 1$ for convenience. The duration of the time analysis is set to $T = 13$, namely before the first reflection, to compare the numerical solutions with the exact one given in [39]. Only the domain $[0,15] \times [0,15]$ is considered due to symmetry. A uniform discretization of the domain is used so that $\Delta x = \Delta y$.

This transient wave propagation problem has been extensively studied in the work of Bathe et al. [11,15,40,41] to investigate the numerical behavior of various time integration schemes, and especially to demonstrate the good filtering properties of the Bathe method (see Section 2.6). The sudden impact, concentrated at the center, generates radial waves with sharp displacement variations, resulting in spurious numerical oscillations. This use case is even more stringent within the PGD framework because of the low rank approximation challenge evoked in Section 2.2 to capture circular structures with a space separation.

We compare the numerical results with three different time integration schemes when refining the mesh: the central difference method (CDM), the Newmark trapezoidal rule (TR) and Bathe method. The time step Δt is constant through the simulation and selected according to each time integration scheme to reduce at best the dissipation and dispersion errors [11]. This is done by setting the so-called CFL number defined by $\text{CFL} = c\Delta t/\Delta x$ to the following recommended values: $\text{CFL} = 1$ for CDM, $\text{CFL} = 0.65$ for TR, and $\text{CFL} = 1$ for Bathe method.

Fig. 3a presents the numerical results obtained with the finite element method. As reported in [40] the central difference method is not effective on this problem for computing accurate solutions: numerous spurious oscillations are visible. As expected, the accuracy is even worse when considering oblique propagation angles with respect to

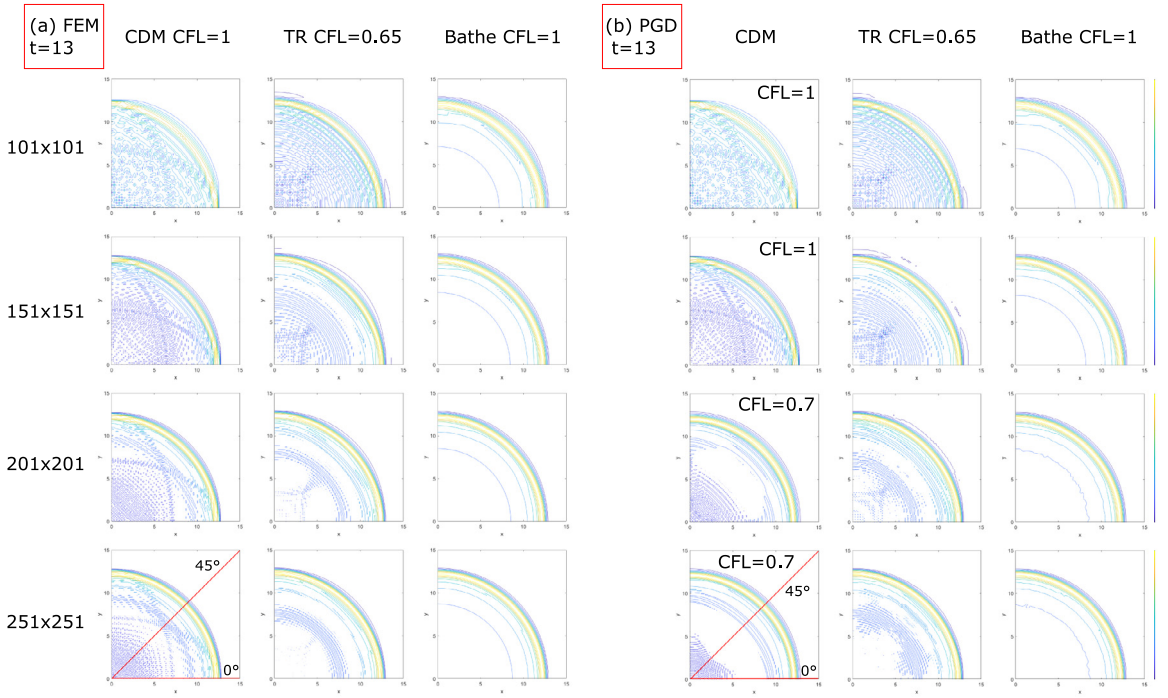

Fig. 3. Transverse displacement field computed with (a) FEM and (b) PGD at the end of the simulation. Mesh convergence depending on selected time integration scheme. CDM: Central Difference Method. TR: Newmark Trapezoidal Rule.

Table 1
Relative error with respect to the exact solution and discrepancy between PGD/FEM solutions. Indicated values are computed with a 2-norm on the nodal points of the 251 by 251 mesh at the end of the simulation (t = 13).

	Error FEM/exact	Error PGD/exact	Discrepancy PGD/FEM
CDM (CFL = 0.7)	7.3%	6.7%	5.7%
TR (CFL = 0.65)	5.8%	5.9%	2.0%
Bathe (CFL = 1)	3.1%	3.3%	0.53%

the mesh orientation. The implicit TR scheme performs better than CDM but spurious oscillations are still visible, especially at the propagation angle $\theta = 45°$. The Bathe method removes these spurious oscillations, even with the coarse 101 by 101 mesh. However, it should be noted that when similar time increments are used, implicit schemes are more expensive than explicit ones in terms of memory and computation time. Also, spurious oscillations can be damped with explicit schemes with specific methods, such as the bulk viscosity method and the Tchamwa–Wielgosz method [42].

Fig. 3b presents the numerical results obtained with the proposed PGD formulation. The stagnation and enrichment criteria (17)–(18) are set equal to $\epsilon = \tilde{\epsilon} = 10^{-3}$. The FEM recommended values of the CFL are used for the trapezoidal rule (0.65) and Bathe method (1), but the PGD solution does not converge with the central difference method if the CFL number is not reduced (down to 0.7 with the finest mesh). Interestingly, with the finest mesh it is observed that the spurious oscillations are rather concentrated at low propagation angles with the PGD while it is the opposite with the FEM. Fig. 4 compares the PGD, FEM and exact solutions at the propagation angles $\theta = 0°$ and $\theta = 45°$. The PGD solution provides the same level of error than its FEM counterpart (see Table 1). For instance, with the 251 by 251 mesh, and with Bathe method, the relative error with respect to the exact solution at the end of the simulation is around 3% for both the PGD and the FEM solutions. The discrepancy between the PGD solution and its FEM counterpart is less than 1%.

Fig. 5a displays the evolution of the number of modes $M(t)$ of the PGD solutions with the different time integration schemes with the 251 by 251 mesh. For each time integration scheme, $M(t)$ monotonically increases,

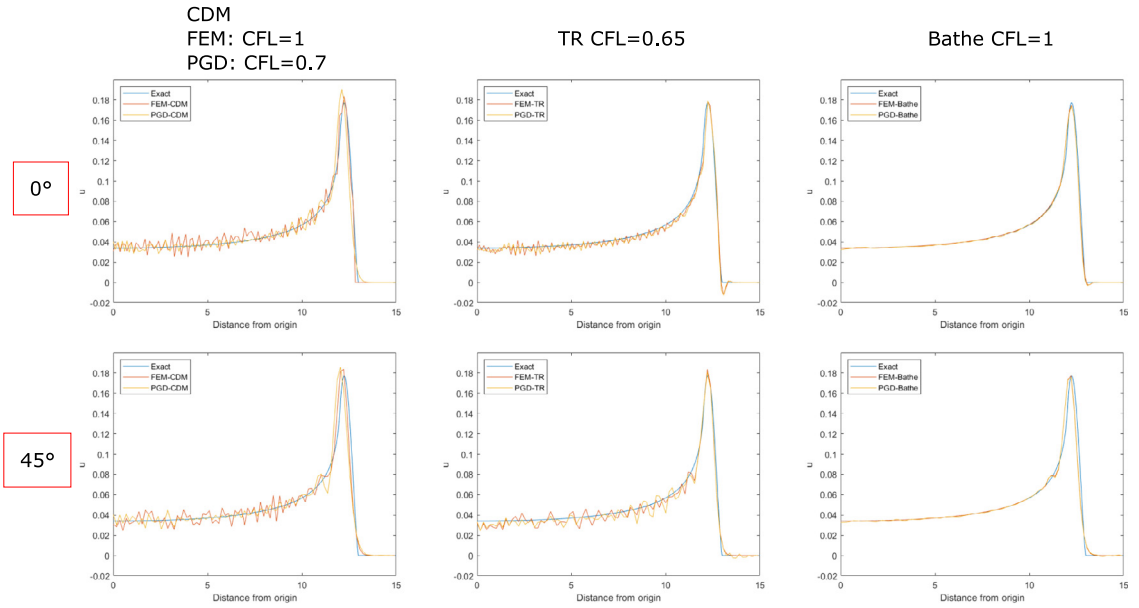

Fig. 4. Comparison of the numerical solutions (251 by 251 mesh) with the exact solution at different propagation angles ($\theta = 0°$ and $\theta = 45°$) at the end of the simulation (t = 13).

but up to different values (57 with CDM, 75 with TR and 32 with Bathe method). This observation agrees with the fictive situation studied in Section 2.2: $M(t)$ increases as the waves expand in the domain. It is also observed that the less the numerical solution exhibits spurious oscillations, the lesser number of modes are required to represent the solution with a separated form. Consequently, the Bathe method provides the lowest number of modes in the PGD solution. Fig. 5b displays the evolution of the mean number of modes $\overline{M}$ when the mesh is refined with the three time integration schemes. It is observed that $\overline{M}$ stabilizes with Bathe method when the mesh is fine enough (below 20), indicating that a limited number of modes is actually sufficient to represent the solution. It follows that more accurate solutions, obtained by refining the mesh, are computed with a higher storage gain. The storage gain reaches 6.7 with Bathe method with the 251 by 251 mesh (see Fig. 5c).

3.3. Water ripple propagation

We consider here the propagation of a ripple in a rectangular pond of water and we focus on the numerical behavior of the PGD solution on long time analyses, with multiple wave reflections on the boundaries. This situation is described by imposing an initial displacement profile (see Fig. 6) and by considering free boundaries:

$$\begin{cases} \frac{1}{c^2}\ddot{u} - \Delta u = 0 & \text{for } (x, y, t) \in \Omega \times]0, T] \\ \frac{\partial u}{\partial n} = 0 & \text{for } (x, y, t) \in \Gamma \times]0, T] \\ u(x, y, 0) = e^{-2(x^2+y^2)}, \dot{u}(x, y, 0) = 0 & \text{for } (x, y) \in \Omega \end{cases} \tag{29}$$

The spatial domain is the same as with the previous use case, the wave velocity is also set to $c = 1$, but we consider a time analysis duration of $T = 6L/c = 180$, giving rise to multiple wave reflections and crossings. A preliminary mesh convergence study showed that a 201 by 201 mesh with the Newmark trapezoidal rule (CFL = 0.65) is sufficient to provide numerical results with acceptable accuracy. This configuration does not generate spurious oscillations as with the previous use case. Fig. 7 compares the wave fields computed by the PGD and its FEM counterpart at time $t = 13$, namely just before the first reflection. The solution consists in a donut-shaped ripple (positive front followed by a negative front) propagating from the center of the pond to the boundaries and reflecting multiple times.

Fig. 8a shows the evolution of the number of modes $M(t)$ through the simulation depending on the mesh refinement. The parameters $\epsilon = \tilde{\epsilon} = 10^{-3}$ are used in the PGD algorithm. For the two coarser meshes, $M(t)$

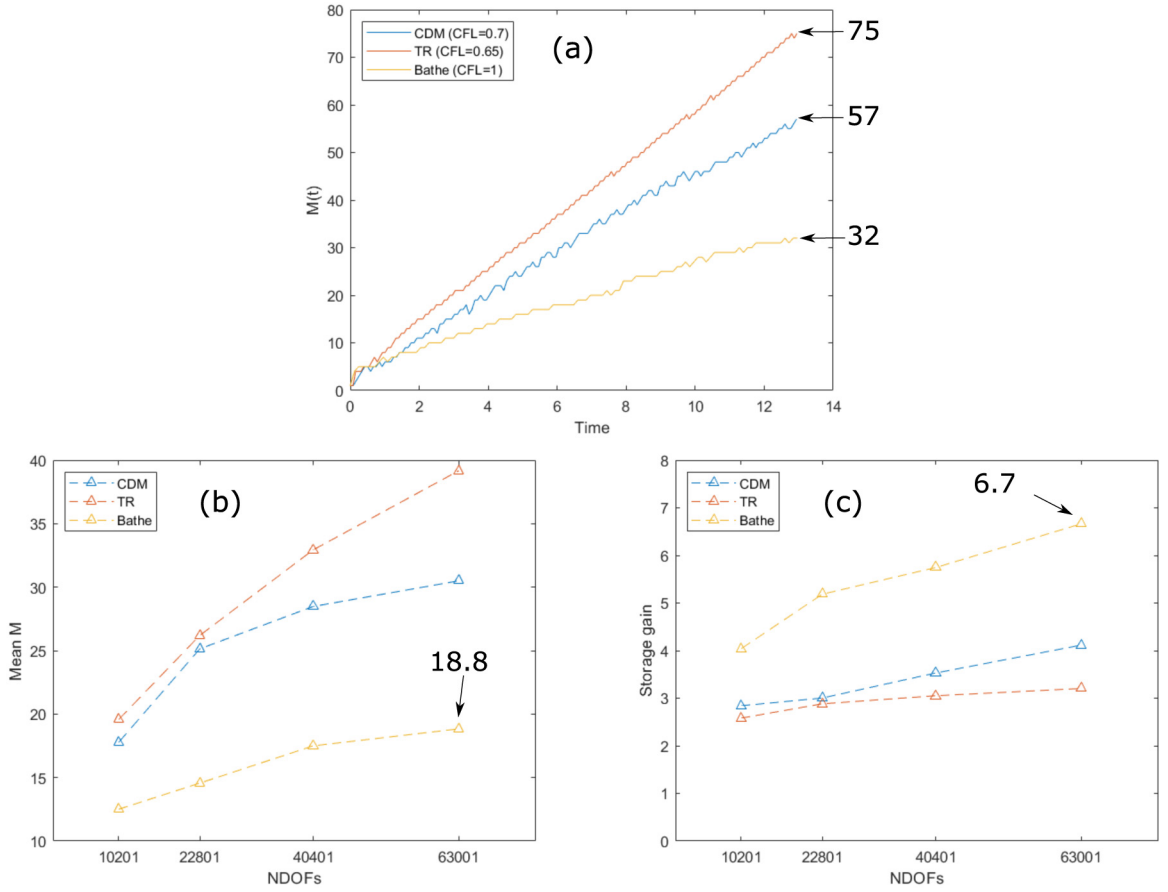

Fig. 5. Evolution of (a) the number of modes $M(t)$ through the simulation, (b) the mean number of modes $\overline{M}$ depending on the mesh, (c) the storage gain as defined by formula (6) depending on the mesh.

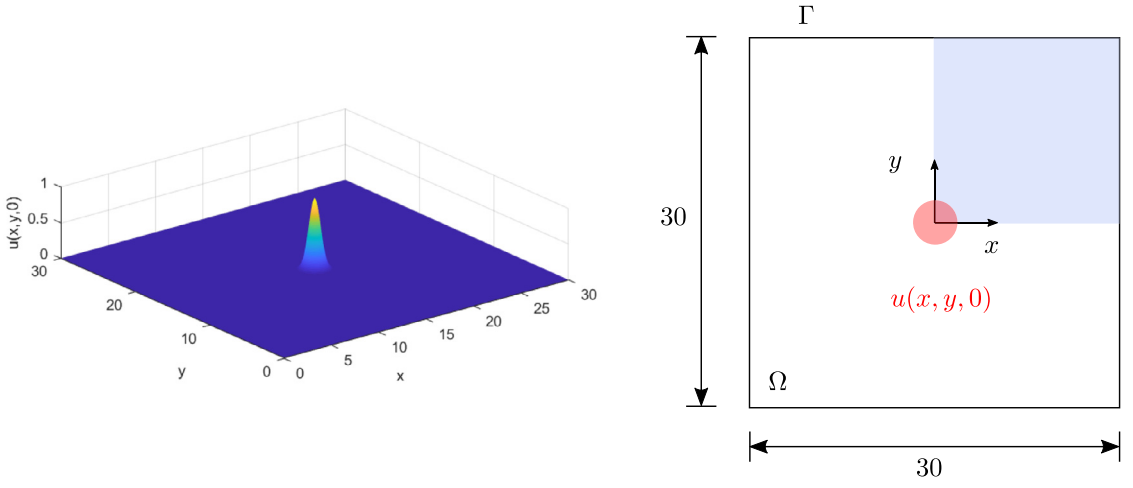

Fig. 6. Initial displacement profile (left) imposed at the center of the domain (right). Numerical results are displayed on the blue area.

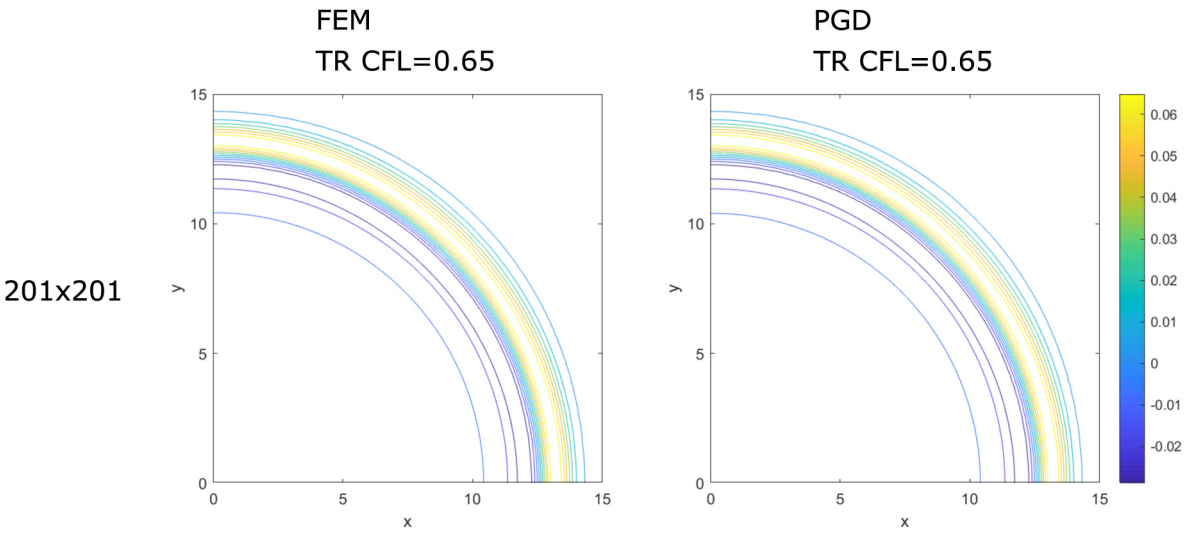

Fig. 7. Transverse displacement field at $t = 13$ computed with the FEM (left) and the PGD (right) by using the trapezoidal rule (CFL $=$ 0.65) and a 201 by 201 mesh.

linearly increases from 0 to 23–25 and then stabilizes around 25. This observation suggests that the maximum number of modes is rather linked to the waves expansion in the domain than to the complexity of the wave field, since numerous wave reflections and crossings occur during this simulation (see Fig. 9).

However, it is observed that the finest the mesh is, the sooner the $M(t)$ curve starts increasing again (see Fig. 8a). This numerical behavior is removed by reducing the enrichment criterion $\tilde{\epsilon}$, as depicted on Fig. 8b and c. However reducing $\tilde{\epsilon}$ too much increases the mean number of modes, which reduces the storage gain. In summary, it can be concluded that around 30 modes are in essence sufficient to represent the solution on the complete time interval, regardless how fine the mesh is (even if it means reducing the enrichment criterion $\tilde{\epsilon}$).

3.4. Laser shock on a metallic target

We now consider a 2D transient elastodynamic problem similar to a laser shock on a metallic target. The objectives are to capture wave conversion phenomena and to study the influence of the space–time concentration of the pressure loading on the numerical behavior of the PGD solution.

The displacement field has two components $u(x, y, t)$ and $v(x, y, t)$ gathered in the displacement field $\underline{u} = (u, v)$. The studied configuration, illustrated on Fig. 10, consists in a rectangular homogeneous linear elastic media under plane strain deformation and small perturbation, subjected to a disymmetric pressure loading on the portion Γ of the top edge. Due to symmetry, only half of the target is considered by imposing a null displacement $v = 0$ along the middle axis of the real target. The displacement field of this problem is governed by the following set of equations:

$$\begin{cases} \rho\ddot{\underline{u}} + \underline{div}\left(\underline{\underline{\sigma}}\right) = \underline{0} & \text{for } (x, y, t) \in \Omega\times]0, T] \\ \frac{\partial u}{\partial n} = p(0, y, t) & \text{for } (x, y, t) \in \Gamma\times]0, T] \\ v(x, 0, t) = 0 & \text{for } (x, t) \in [0, H]\times]0, T] \\ \underline{u}(x, y, 0) = \underline{0}, \dot{\underline{u}}(x, y, 0) = \underline{0} & \text{for } (x, y) \in \Omega \end{cases} \tag{30}$$

where $\underline{\underline{\sigma}}$ is the Cauchy's stress tensor. The pressure loading is under the separated form $p(0, y, t) = f(t)g(y)$ with the time and spatial profiles depicted on Fig. 10. The simulation parameters are presented in Table 2. The PGD operators of this problem are derived with the methodology presented in the Appendix.

Fig. 11 shows snapshots of the displacement field computed with the proposed PGD method with Newmark trapezoidal rule (CFL $= 0.65$). It is also observed with this use case that $M(t)$ increases as the two components of the waves fill the domain, and then $M(t)$ stabilizes (below 20). Fig. 12 compares snapshots of $u(x, 0, t)$ and $u(0, y, t)$

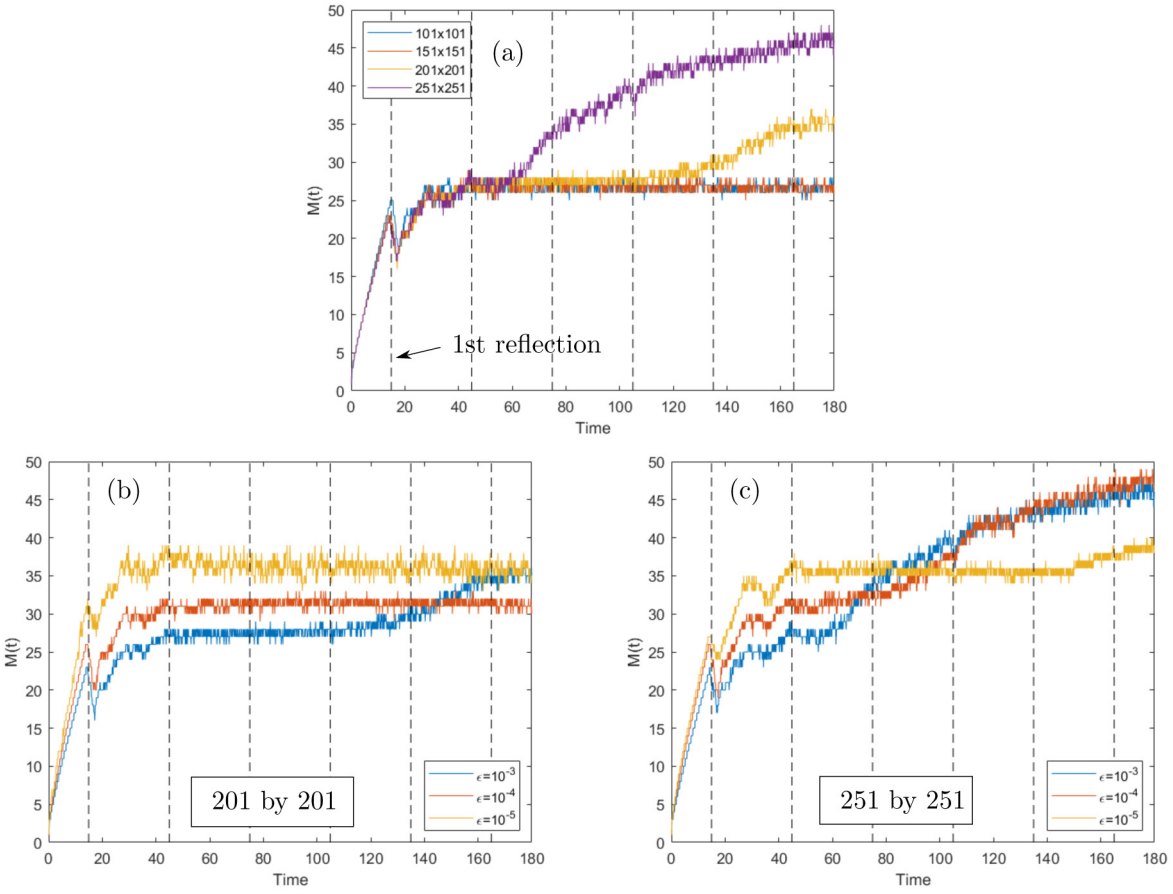

Fig. 8. Evolution of the number of modes $M(t)$ through the simulation depending on (a) the mesh refinement and (b-c) the enrichment criterion.

Table 2
Simulation parameters.

E [GPa]:	70
ν:	0.33
ρ [kg/m^3]:	2700
H [mm]:	10
W [mm]:	15
T_s [µs]:	1.32
r [mm]:	2
T [µs]:	3.23
Δt [ns]:	4.87
N_x:	100
N_y:	150
ϵ:	10^{-4}
$\tilde{\epsilon}$:	10^{-4}

computed with the PGD and with its FEM counterpart. The discrepancy between the PGD and the FEM solutions is larger near $x = H$. Our interpretation is that the free boundary condition at $x = H$ doubles the displacement magnitude, leading to sharper variations of the displacement field that are more difficult to be captured by the PGD solution.

The applied loading in x-direction generates a 2D displacement field propagating in the medium. As expected, the applied pressure pushes Γ downwards, which generates a compressive longitudinal wave propagating in x-direction and a transverse wave propagating in y-direction (left column). The speed of the longitudinal and

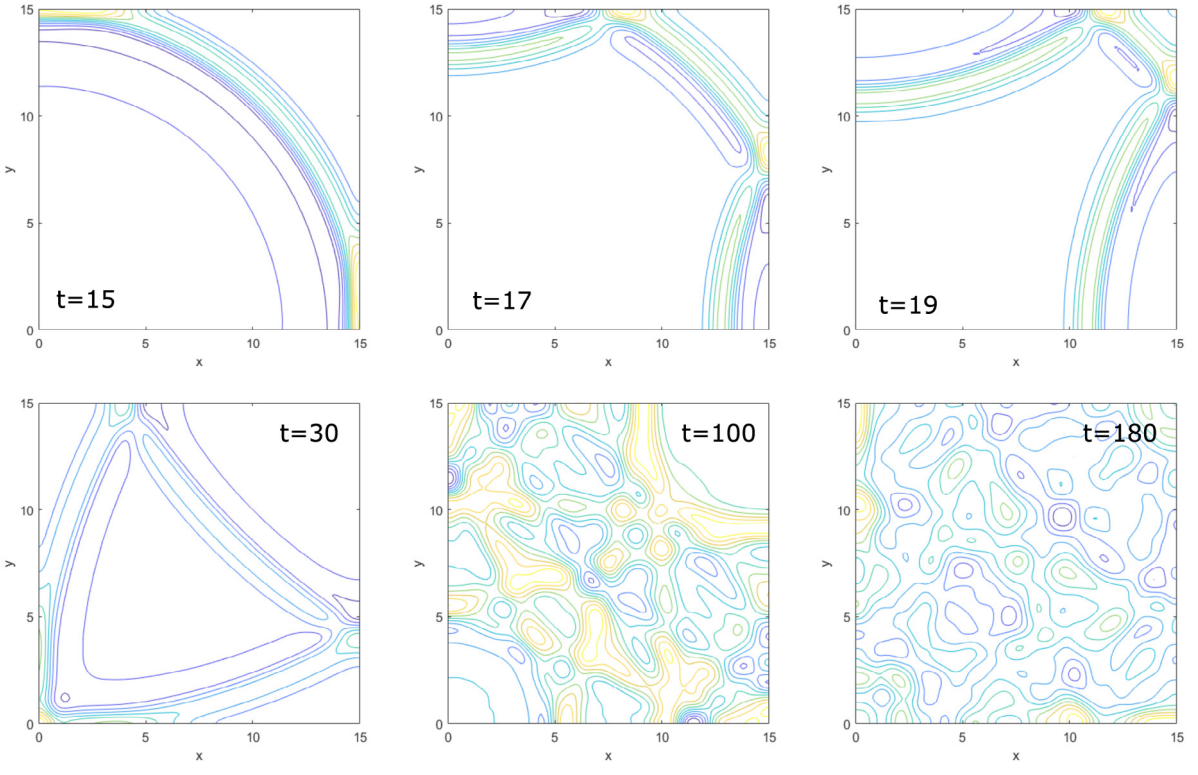

Fig. 9. Snapshots of the transverse displacement field computed with the PGD by using the trapezoidal rule (CFL = 65) and the 201 by 201 mesh.

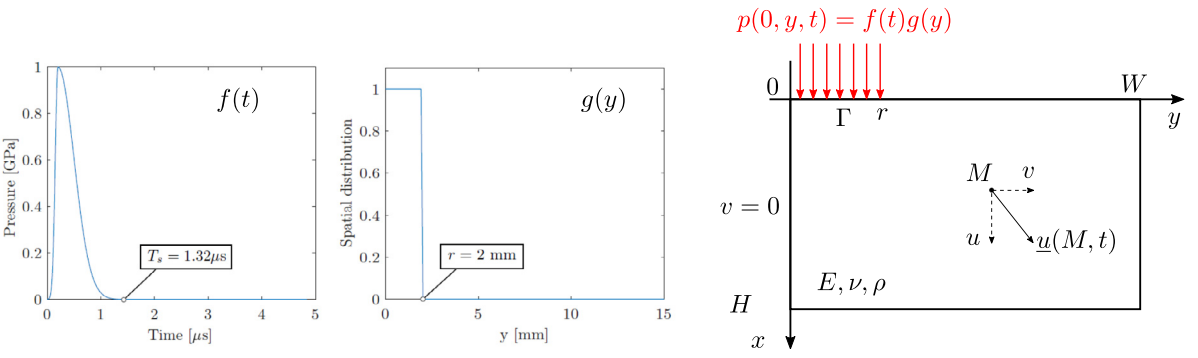

Fig. 10. Laser shock on a metallic target. Half of the domain is computed by imposing $v = 0$ on the left edge (corresponding to the middle axis of the real target).

transverse waves can be roughly evaluated by dividing the distance traveled during a given time interval ΔT. The uncertainty on the velocity estimation is given by $2\Delta x/\Delta T$, where Δx is the spatial discretization and $2\Delta x$ represents the maximum error on the distance approximation with this technique. With the selected parameters ($\Delta T = 360\Delta t, \Delta x = \Delta y = 0.1$mm) the confidence interval on the velocity estimations is ± 114 m/s. It gives 6200 ± 114 m/s for the longitudinal wave propagating along the x-axis, which agrees well with the theoretical value $c_L = 6198$ m/s. And it gives 3100 ± 114 m/s for the transverse wave propagating along the y-axis, which is also consistent with the theoretical value $c_T = 3122$ m/s.

Then the compressive wave propagating along the x-axis progressively initiates waves propagating in y direction. There are two contributions to this effect. First, the initial disturbance progressively expands diagonally (compare

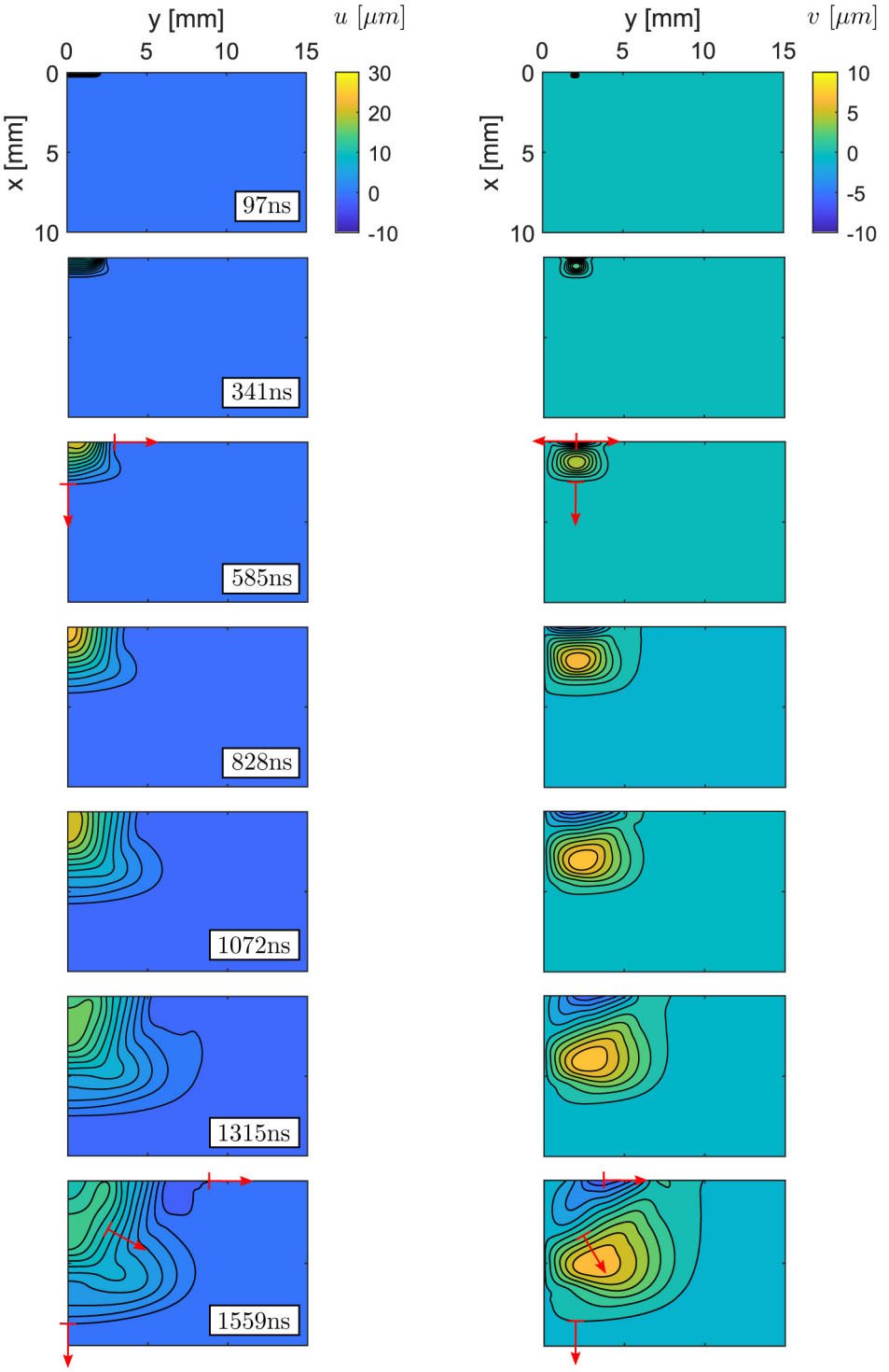

Fig. 11. Snapshots of the 2D displacement field (Newmark trapezoidal rule with CFL $= 0.65$). The red arrows represent the propagation direction of the wave fronts. Left column: component u. Right column: component v.

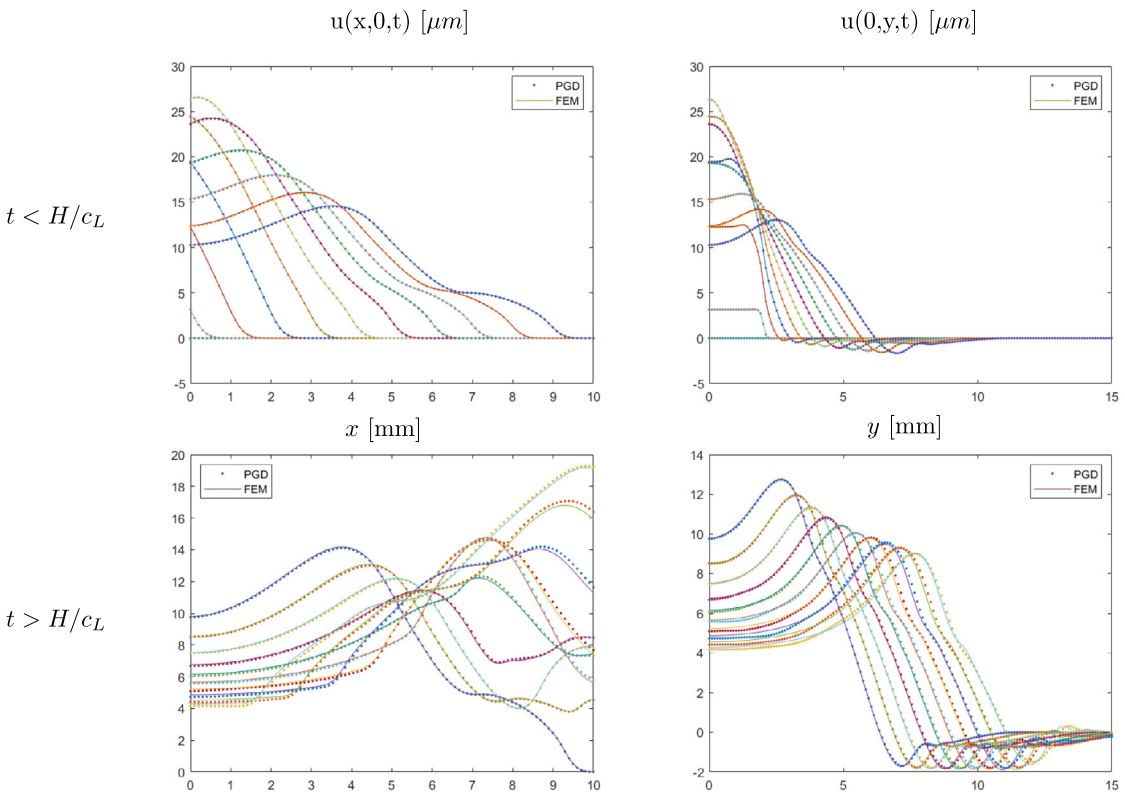

Fig. 12. Snapshots of $u(x, 0, t)$ (left) and $u(0, y, t)$ (right) before the first reflection at $x = H$ (top) and after (bottom).

the propagation directions indicated by the red arrows at $t = 585$ ns and $t = 1559$ ns). This is due to the conversion of the longitudinal wave propagating along the x-axis into transverse waves propagating along the y-axis. Second, the compression front propagating in x-direction locally pushes the material in y-direction, just as a compressed elastic bar clamped at $y = 0$ and free at $y = r$ would extend its length (Poisson effect). As depicted on Fig. 12 (top left image), this wave conversion results in a progressive decay of the amplitude of the initial compressive wave propagating along the x-axis.

We now investigate the influence of the pressure loading concentration in space or in time. To do so, we consider pressure loadings with a symmetric half-sine time profile. Fig. 13a shows the evolution of the mean number of modes $\overline{M}$ by varying the ratio $T_s/(H/c_L)$ with $r/W = 0.3$. The shorter the impact duration is, the higher the mean number of modes. This is because the displacement wave fronts become sharper as the duration of the impact decreases. It results that the storage gain increases as the impact duration increases. Fig. 13b shows the same data by varying the ratio r/W with $T_s/(H/c_L) = 1$. The influence of the space concentration is less noticeable than the time concentration, but it is observed that the mean number of modes increases as r diminishes. This is because the waves become more radial if the impact is concentrated in space hence more difficult to be captured with the space variables separation. With $T_s/(H/c_L) = 1$ and $r/W = 0.3$ the mean number of modes is 8.6 and the corresponding storage gain is 7.

3.5. Computation time per time step

Although the proposed method has been implemented on 2D use cases, with stringent loading configurations for the space separation, the following results are promising for addressing computationally intensive 3D problems in future work. We compare hereunder the calculation time to compute the PGD solutions and their FEM counterparts. The simulations are run with Matlab R2018a on a laptop with a single core Intel i7-5500U 2.40 GHz CPU and 8 GB RAM. We focus on the CPU time per time step in the time incremental resolution.

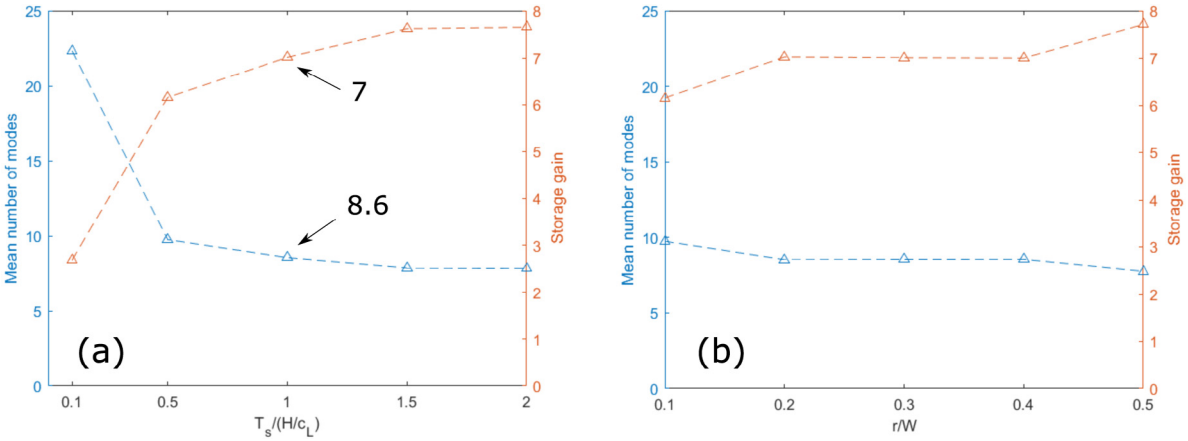

Fig. 13. Evolution of the mean number of modes and storage gain depending on the loading concentration (a) in time or (b) in space.

Table 3
CPU times required to solve the 2D transient wave propagation problems. For the first use case the percentage under parenthesis indicates the relative error with respect to the exact solution at the end of the simulation. The Bathe method is used for the membrane problem with CFL=1, the Newmark trapezoidal rule is used for the water ripple and laser shock problems with CFL=0.65.

Use case	NDOFs	FEM	PGD			CPU gain[a]
		CPU time per time step (s) (number of increments)	CPU time per time step (s)			
			$k = 10$	$k = 50$	$k = \infty$	
Membrane	63,001	1.1 (109) (<4%)	0.22 (<4%)	0.26 (<4%)	0.30 (<4%)	5.0
Water ripple	40,401	0.31 (1847)	0.14	0.19	0.26	2.2
Laser shock	30,000	0.46 (306)	0.14	0.16	0.17	3.3

[a]The CPU gain is computed as the ratio between the CPU time per time step to compute the FEM solution and the PGD solution with $k = 10$.

Table 3 summarizes the CPU times per time step obtained for all the use cases by varying the maximum number of iterations in the stagnation loop ($k = 10, 50, \infty$). The relative error with respect to the exact solution can be computed for the first use case. It can be seen that $k = 10$ iterations are sufficient to compute numerical solutions as accurate as with $k = \infty$. Hence the proposed PGD method speeds up the calculations without decreasing the accuracy, and leads to lighter solutions in terms of storage (see Fig. 5c).

Fig. 14 compares the evolution of the CPU time per time step for the first use case depending on the time integration scheme. With the PGD, it is observed that for all the time integration schemes the CPU time per time step linearly increases with the number of degrees of freedom (NDOFs), which is not the case with the FEM. The exception is with the explicit time integration scheme, namely with the central difference method, as explained in Section 2.6. The PGD is more efficient when using implicit time integration schemes for which consistent matrices are inverted. The CPU time per time step is reduced by 5 with Bathe method and the finest mesh (63,001 DOFs).

Two aspects contribute to the reduction of the CPU time per time step. First, the proposed method lowers the complexity of the resolution by solving multiple 1D problems in space rather than a single 2D problem. Second, the space separation strategy reduces the memory consumption. Indeed, the solutions at previous time steps, involved in the right hand side of Eq. (15) due to the time discretization, are stored under separated form, which are lighter than full 2D representations if the number of modes is small enough. In addition, when using implicit time schemes, the contribution of the stiffness matrix to the left hand side operator is also stored under separated form, within the operators B_1^i and B_2^i in Eq. (15), of sizes $N_x \times M_j$ and $N_y \times M_j$, respectively, with $j = k-1, k-2$.

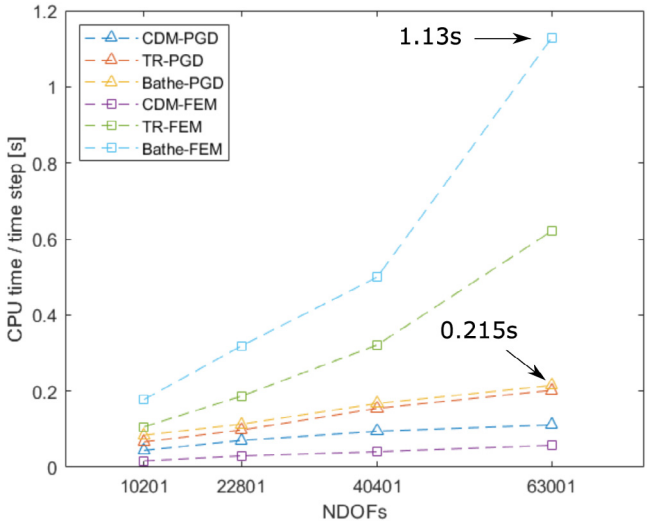

Fig. 14. CPU time per time step for the simulations on the first use case (see Section 3.2). PGD solutions are computed with $\tilde{\epsilon} = 10^{-3}$ and a limited number of iterations in the stagnation loop ($k = 10$).

4. Conclusion

In this work, we proposed a time adaptive space separation strategy to solve transient wave propagation problems in separable domains. The separated form representation of the solution is computed on the fly with a PGD algorithm ran at each time increment. The numerical results show that the PGD solution is enriched when needed, as the waves are generated by the loading and travel in the domain. The number of modes in the PGD solution stabilizes when long time analyses are considered. The time integration scheme should be carefully selected to avoid spurious high frequency oscillations, leading to an increased number of modes. For all the studied use cases, either on the 2D scalar wave equation or on the 2D elastodynamic equations, the proposed method computes the solution faster and with less storage capacities than the standard finite element method. Besides, the number of modes stabilizes when refining the mesh, indicating that the storage gain increases when richer solutions are computed.

Future work will be conducted in the following directions to improve the performances. First, it could be interesting to use the spectral element method instead of the finite element method for the spatial discretization. The spatial accuracy of the PGD solution would be significantly improved by increasing the order of the interpolants, leading to less spurious oscillations, hence to a lower number of modes. Therefore, the memory consumption and the storage needs would be reduced even more. Besides, the spectral elements could be defined on the Gauss–Lobatto–Legendre (GLL) points to diagonalize the left hand side operator that needs to be inverted at each time step, within the enrichment and stagnation loops. The complexity of the resolution would be reduced and so would be the computation time. Second, although the proposed method has been implemented on 2D use cases only, the numerical behavior is promising for future applications on 3D transient wave propagation problems. Indeed, the crucial ingredient is the space separation, which could speed up calculations associated to rich solutions on nowadays engineered materials, involving thin geometries sometimes composed of extremely fine plies. Either a 2D/1D or a 1D/1D/1D space separation strategy could be considered. Finally, the proposed method could be extended to parametric studies on wave propagation problems, to circumvent the so-called curse of dimensionality when it comes to solve high dimension problems. To be consistent with the proposed time incremental approach, a possible implementation could be to run a standard parametric PGD algorithm at each time step.

Declaration of competing interest

The authors declare that they have no known competing financial interests or personal relationships that could have appeared to influence the work reported in this paper.

Acknowledgments

This work was supported by a government funding under the project FUI, France MONARQUE.

Appendix

We derive herein the PGD operators associated to the 2D wave propagation problem presented in Section 2.4. The same methodology can be used for deriving the operators associated to the elastodynamic problem studied in Section 3.4. More details regarding the manipulation of a multi-component displacement field $\underline{u} = (u, v)$ within a PGD framework can be found in [32].

A.1. Left hand side operators

Let us note $\mathcal{P} = \int_{\Omega_x} P P^T$ and $\mathcal{Q} = \int_{\Omega_y} Q Q^T$. Now let us introduce the finite element discretization (11)–(12) in the left hand side of Eq. (14):

$$\begin{aligned}\int_\Omega u^* \phi \psi &= \int_{\Omega_x} \phi^* \phi \times \int_{\Omega_y} \psi \psi \\ &= \left((\Phi^*)^T \left[\int_{\Omega_x} P P^T \right] \Phi \right) \times \left(\Psi^T \left[\int_{\Omega_y} Q Q^T \right] \Psi \right) \\ &= (\Phi^*)^T \left(\Psi^T \mathcal{Q} \Psi \right) (\mathcal{P} \Phi) \end{aligned} \tag{31}$$

A.2. Right hand side operators

We proceed similarly with each term of the right hand side of Eq. (14). The following property is used to present under compact form the terms associated to u_{n-1}^{k+1}, u^k and u^{k-1}:

$$\sum_{i=1}^{M} \left[a^T A b_i \right] \times \left[c^T B d_i \right] = a^T \left(A \mathcal{B} \right) \left(B \mathcal{D} \right)^T c \tag{32}$$

where $\mathcal{B} = [b_1|...|b_M]$ and $\mathcal{D} = [d_1|...|d_M]$. Let us use the notation $\mathcal{X}^k = \left[\Phi_1^k | ... | \Phi_{M_k}^k \right]$ and $\mathcal{Y}^k = \left[\Psi_1^k | ... | \Psi_{M_k}^k \right]$. Then the different contributions to the right hand side are:

$$-\int_\Omega u^* u_{n-1}^{k+1} = (\Phi^*)^T \left(-\mathcal{P} \mathcal{X}_{n-1}^{k+1} \right) \left(\mathcal{Q} \mathcal{Y}_{n-1}^{k+1} \right)^T \Psi \tag{33}$$

$$+2\int_\Omega u^* u^k = (\Phi^*)^T \left(2\mathcal{P} \mathcal{X}^k \right) \left(\mathcal{Q} \mathcal{Y}^k \right)^T \Psi \tag{34}$$

$$-\int_\Omega u^* u^{k-1} = (\Phi^*)^T \left(-\mathcal{P} \mathcal{X}^{k-1} \right) \left(\mathcal{Q} \mathcal{Y}^{k-1} \right)^T \Psi \tag{35}$$

$$+\int_\Omega (c\Delta t)^2 u^* f^k = (\Phi^*)^T \left((c\Delta t)^2 \int_{\Omega_x} P g^k \right) \left(\int_{\Omega_y} Q h^k \right)^T \Psi \tag{36}$$

Now let us introduce $\mathcal{P}_{,xx} = \int_{\Omega_x} P'(P')^T$ and $\mathcal{Q}_{,yy} = \int_{\Omega_y} Q'(Q')^T$. Then the remaining term of the right hand side is:

$$-\int_\Omega (c\Delta t)^2 \nabla u^* \nabla u^k = (\Phi^*)^T \left(-(c\Delta t)^2 \mathcal{P}_{,xx} \mathcal{X}^k \right) \left(\mathcal{Q} \mathcal{Y}^k \right)^T \Psi \tag{37}$$

$$+ (\Phi^*)^T \left(-(c\Delta t)^2 \mathcal{P} \mathcal{X}^k \right) \left(\mathcal{Q}_{,yy} \mathcal{Y}^k \right)^T \Psi \tag{38}$$

References

[1] R. Fabbro, P. Peyre, L. Berthe, X. Scherpereel, Physics and applications of laser-shock processing, J. Laser Appl. 10 (6) (1998) 265–279, http://dx.doi.org/10.2351/1.52186.

[2] C. Bolis, L. Berthe, M. Boustie, M. Arrigoni, S. Barradas, M. Jeandin, Physical approach to adhesion testing using laser-driven shock waves, J. Phys. D: Appl. Phys. 40 (10) (2007) 3155–3163, http://dx.doi.org/10.1088/0022-3727/40/10/019.
[3] M. Ghrib, L. Berthe, N. Mechbal, M. Rébillat, M. Guskov, R. Ecault, N. Bedreddine, Generation of controlled delaminations in composites using symmetrical laser shock configuration, Compos. Struct. 171 (2017) 286–297, http://dx.doi.org/10.1016/j.compstruct.2017.03.039.
[4] R. Ecault, M. Boustie, F. Touchard, F. Pons, L. Berthe, L. Chocinski-Arnault, B. Ehrhart, C. Bockenheimer, A study of composite material damage induced by laser shock waves, Composites A 53 (2013) 54–64, http://dx.doi.org/10.1016/j.compositesa.2013.05.015.
[5] B. Ehrhart, R. Ecault, F. Touchard, M. Boustie, L. Berthe, C. Bockenheimer, B. Valeske, Development of a laser shock adhesion test for the assessment of weak adhesive bonded cfrp structures, Int. J. Adhes. Adhes. 52 (2014) 57–65, http://dx.doi.org/10.1016/j.ijadhadh.2014.04.002.
[6] M. Sagnard, R. Ecault, F. Touchard, M. Boustie, L. Berthe, Development of the symmetrical laser shock test for weak bond inspection, Opt. Laser Technol. 111 (2019) 644–652, http://dx.doi.org/10.1016/j.optlastec.2018.10.052.
[7] R. Ecault, F. Touchard, L. Berthe, M. Boustie, Laser shock adhesion test numerical optimization for composite bonding assessment, Compos. Struct. 247 (2020) 112441, http://dx.doi.org/10.1016/j.compstruct.2020.112441.
[8] J.P. Cuq-Lelandais, M. Boustie, L. Berthe, T. de Rességuier, P. Combis, J.P. Colombier, M. Nivard, A. Claverie, Spallation generated by femtosecond laser driven shocks in thin metallic targets, J. Phys. D: Appl. Phys. 42 (6) (2009) 065402, http://dx.doi.org/10.1088/0022-3727/42/6/065402.
[9] A. Deraemaeker, I. Babuška, P. Bouillard, Dispersion and pollution of the fem solution for the Helmholtz equation in one, two and three dimensions, Internat. J. Numer. Methods Engrg. 46 (1999) 471–499, http://dx.doi.org/10.1002/(SICI)1097-0207(19991010)46:4<471::AID-NME684>3.0.CO;2-6.
[10] K. Bathe, Finite Element Procedures, second ed., 4th printing, Watertown, MA, 2016.
[11] G. Noh, S. Ham, K.-J. Bathe, Performance of an implicit time integration scheme in the analysis of wave propagations, Comput. Struct. 123 (2013) 93–105, http://dx.doi.org/10.1016/j.compstruc.2013.02.006.
[12] G. Noh, K.-J. Bathe, The bathe time integration method with controllable spectral radius: The $\rho\infty$-bathe method, Comput. Struct. 212 (2019) 299–310, http://dx.doi.org/10.1016/j.compstruc.2018.11.001.
[13] A.T. Patera, A spectral element method for fluid dynamics: Laminar flow in a channel expansion, J. Comput. Phys. 54 (3) (1984) 468–488, http://dx.doi.org/10.1016/0021-9991(84)90128-1.
[14] G. Seriani, S. Oliveira, Dispersion analysis of spectral element methods for elastic wave propagation, Wave Motion 45 (6) (2008) 729–744, http://dx.doi.org/10.1016/j.wavemoti.2007.11.007.
[15] S. Ham, K.-J. Bathe, A finite element method enriched for wave propagation problems, Comput. Struct. 94–95 (2012) 1–12, http://dx.doi.org/10.1016/j.compstruc.2012.01.001.
[16] G.M. Hulbert, T.J. Hughes, Space-time finite element methods for second-order hyperbolic equations, Comput. Methods Appl. Mech. Engrg. 84 (3) (1990) 327–348, http://dx.doi.org/10.1016/0045-7825(90)90082-W.
[17] F. Chinesta, A. Ammar, E. Cueto, Recent advances and new challenges in the use of the proper generalized decomposition for solving multidimensional models, Arch. Comput. Methods Eng. 17 (2010) 327–350, http://dx.doi.org/10.1007/s11831-010-9049-y.
[18] F. Chinesta, A. Leygue, F. Bordeu, J. Aguado, E. Cueto, D. Gonzalez, I. Alfaro, A. Ammar, A. Huerta, PGD-based computational vademecum for efficient design, optimization and control, Arch. Comput. Methods Eng. 20 (2013) 31–59, http://dx.doi.org/10.1007/s11831-013-9080-x.
[19] P. Ladevèze, J.-C. Passieux, D. Nérona, The LATIN multiscale computational method and the proper generalized decomposition, Comput. Methods Appl. Mech. Engrg. 199 (2010) 1287–1296, http://dx.doi.org/10.1016/j.cma.2009.06.023.
[20] A. Chatterjee, An introduction to the proper orthogonal decomposition, Current Sci. 78 (7) (2000) 808–817.
[21] A. Ammar, M. Normandin, F. Daim, D. Gonzalez, E. Cueto, F. Chinesta, Non incremental strategies based on separated representations: Applications in computational rheology, Commun. Math. Sci. 8 (3) (2006) 671–695, http://dx.doi.org/10.1007/s12289-009-0647-x.
[22] B. Favoretto, C. de Hillerin, O. Bettinotti, V. Oancea, A. Barbaruloa, Reduced order modeling via pgd for highly transient thermal evolutions in additive manufacturing, Comput. Methods Appl. Mech. Engrg. 349 (2019) 405–430, http://dx.doi.org/10.1016/j.cma.2019.02.033.
[23] A. Ammar, The proper generalized decomposition: a powerful tool for model reduction, Int. J. Mater. Form 3 (2010) 89–102, http://dx.doi.org/10.1007/s12289-009-0647-x.
[24] A. Ammar, F. Chinesta, Circumventing curse of dimensionality in the solution of highly multidimensional models encountered in quantum mechanics using meshfree finite sums decomposition, in: Lecture Notes on Computational Science and Engineering, Springer, Berlin, 2008, pp. 1–17.
[25] A. Nouy, A priori model reduction through proper generalized decomposition for solving time-dependent partial differential equations, Comput. Methods Appl. Mech. Engrg. 199 (2010) 1603–1626, http://dx.doi.org/10.1016/j.cma.2010.01.009.
[26] A. Falco, A. Nouy, A proper generalized decomposition for the solution of elliptic problems in abstract form by using a functional Eckart–Young approach, J. Math. Anal. Appl. 376 (2011) 469–480, http://dx.doi.org/10.1016/j.jmaa.2010.12.003.
[27] P. Ladevèze, PGD in linear and nonlinear computational solid mechanics, in: Separated Representations and PGD-Based Model Reduction, Springer, 2014, pp. 91–152, http://dx.doi.org/10.1007/978-3-7091-1794-1_3.
[28] N. Shirafkan, F. Bamer, M. Stoffel, B. Markert, Quasistatic analysis of elastoplastic structures by the proper generalized decomposition in a space-time approach, Mech. Res. Commun. (2020) 103500, http://dx.doi.org/10.1016/j.mechrescom.2020.103500.
[29] L. Boucinha, A. Ammar, A. Gravouil, A. Nouy, Ideal minimal residual-based proper generalized decomposition for non-symmetric multi-field models – application to transient elastodynamics in space-time domain, Comput. Methods Appl. Mech. Engrg. 273 (2014) 56–76, http://dx.doi.org/10.1016/j.cma.2014.01.019.

[30] L. Boucinha, A. Gravouil, A. Ammar, Space–time proper generalized decompositions for the resolution of transient elastodynamic models, Comput. Methods Appl. Mech. Engrg. 255 (2013) 67–88, http://dx.doi.org/10.1016/j.cma.2012.11.003.
[31] A. Tveito, R. Winther, Introduction to Partial Differential Equations: A Computational Approach, Springer, Berlin, Heidelberg, 2005, http://dx.doi.org/10.1007/b138016.
[32] G. Quaranta, B. Bognet, R.I. nez, A. Tramecon, E. Haug, F. Chinesta, A new hybrid explicit/implicit in-plane-out-of-plane separated representation for the solution of dynamic problems defined in plate-like domains, Comput. Struct. 210 (2018) 135–144, http://dx.doi.org/10.1016/j.compstruc.2018.05.001.
[33] C. Ghnatios, E. Cueto, A. Falco, J.-L. Duval, F. Chinesta, Spurious-free interpolations for non-intrusive PGD-based parametric solutions: Application to composites forming processes, Int. J. Mater. Form (2020) http://dx.doi.org/10.1007/s12289-020-01561-0.
[34] L. Trefethen, D. Bau, Numerical Linear Algebra, SIAM, 1997.
[35] A. Ammar, F. Chinesta, P. Diez, A. Huerta, An error estimator for separated representations of highly multidimensional models, Comput. Methods Appl. Mech. Engrg. 199 (25) (2010) 1872–1880, http://dx.doi.org/10.1016/j.cma.2010.02.012.
[36] E. Nadal, F. Chinesta, M. Beringhier, J. Ródenas, F. Fuenmayor, A separated representation of an error indicator for the mesh refinement process under the proper generalized decomposition framework, Comput. Mech. 55 (2015) 251–266, http://dx.doi.org/10.1007/s00466-014-1097-y.
[37] I. Alfaro, D. Gonzalez, S. Zlotnik, P. Diez, E. Cueto, F. Chinesta, An error estimator for real-time simulators based on model order réduction, Adv. Modelling Simul. Eng. Sci. (2015) 2,30, http://dx.doi.org/10.1186/s40323-015-0050-8.
[38] S.R. Wu, Lumped mass matrix in explicit finite element method for transient dynamics of elasticity, Comput. Methods Appl. Mech. Engrg. 195 (44) (2006) 5983–5994, http://dx.doi.org/10.1016/j.cma.2005.10.008.
[39] B. Yue, M.N. Guddatia, Dispersion-reducing finite elements for transient acoustics, J. Acoust. Soc. Am. 118 (2005) 2132, http://dx.doi.org/10.1121/1.2011149.
[40] G. Noh, K.-J. Bathe, An explicit time integration scheme for the analysis of wave propagations, Comput. Struct. 129 (2013) 178–193, http://dx.doi.org/10.1016/j.compstruc.2013.06.007.
[41] K.-T. Kim, L. Zhang, K.-J. Bathe, Transient implicit wave propagation dynamics with overlapping finite elements, Comput. Struct. 199 (2018) 18–33, http://dx.doi.org/10.1016/j.compstruc.2018.01.007.
[42] L. Maheo, V. Grolleau, G. Rio, Numerical damping of spurious oscillations: a comparison between the bulk viscosity method and the explicit dissipative tchamwa–Wielgosz scheme, 2013, p. 109,128, http://dx.doi.org/10.1007/s00466-012-0708-8.